

# Photon helicity driven electric currents in graphene

J. Karch<sup>1</sup>, P. Olbrich<sup>1</sup>, M. Schmalzbauer<sup>1</sup>, C. Brinsteiner<sup>1</sup>, U. Wurstbauer<sup>1</sup>, M. M. Glazov<sup>2</sup>, S. A. Tarasenko<sup>2</sup>, E. L. Ivchenko<sup>2</sup>, D. Weiss<sup>1</sup>, J. Eroms<sup>1</sup>, and S. D. Ganichev<sup>1</sup>

<sup>1</sup> *Terahertz Center, University of Regensburg, 93040 Regensburg, Germany and*

<sup>2</sup> *Ioffe Physical-Technical Institute, Russian Academy of Sciences, 194021 St. Petersburg, Russia*

We report on the observation of photon helicity driven currents in graphene. The directed net electric current is generated in single layer graphene by circularly polarized terahertz laser radiation at normal as well as at oblique incidence and changes its sign upon reversing the radiation helicity. The phenomenological and microscopic theories of the observed photocurrents are developed. We demonstrate that under oblique incidence the current is caused by the circular photon drag effect in the interior of graphene sheet. By contrast, the effect at normal incidence stems from the sample edges, which reduce the symmetry and result in an asymmetric scattering of carriers driven by the radiation field. Besides a photon helicity dependent current we also observe photocurrents in response to linearly polarized radiation. The microscopic mechanisms governing this effect are discussed.

PACS numbers: 73.50.Pz, 72.80.Vp, 81.05.ue, 78.67.Wj

## I. INTRODUCTION

Graphene, a one-atom-thick layer of graphite, was experimentally isolated only six years ago and has since then revealed fascinating effects in a number of experiments owing to specifics of the electron energy spectrum<sup>1</sup>. The chiral motion of charge carriers leads to a peculiar modification of the quantum Hall effect<sup>2,3</sup> and plays an important role in phase-coherent phenomena such as, e.g., weak localization<sup>4,5</sup>. The fact that the band structure resembles the dispersion relation of a massless relativistic particle has created enormous excitement since relativistic experiments in a solid state environment became feasible<sup>6</sup>. Indeed, Klein tunneling<sup>7</sup>, a relativistic effect predicted over 80 years ago<sup>8</sup>, has been experimentally demonstrated very recently in gated graphene structures<sup>9</sup>. Another characteristic feature of graphene is the presence of two valleys, each containing a Dirac cone. This constitutes a two-state degree of freedom – much like the electron spin – which was suggested to be applied in valleytronics<sup>10</sup>. Most recently several theoretical groups suggested that the combination of intense radiation and a constant electric field applied to single or multilayer graphene may result in the generation of a valley-polarized<sup>12,13</sup> and anomalous Hall current<sup>11</sup>.

Here we demonstrate that the illumination of monolayer graphene by radiation of a terahertz (THz) laser in the absence of any *dc* field applied to the sample causes directed electric currents, including those solely driven by the radiation helicity. Photon helicity driven currents are well known in semiconductor low-dimensional structures, and the photocurrent generation has been proven to be a very efficient method to study non-equilibrium processes in semiconductors yielding information on their symmetry, details of the band structure and processes of electron momentum, spin and energy relaxation, etc.<sup>14–17</sup>. Microscopic mechanisms of this class of phenomena in quantum wells are based on spin-orbit coupling in gyrotropic materials<sup>14,18,19</sup> or on orbital effects originated from the

quantum interference of optical transitions<sup>20–22</sup>. Our experiments evidence that the helicity driven photocurrent in graphene consists of two contributions. One of them appears at oblique incidence only and is an odd function of the angle of incidence. The other has its maximum at normal incidence and is an even function of the incidence angle. We show that the first effect is caused by the circular photon drag effect<sup>23–26</sup>, see also Ref. 27, which stems from the simultaneous transfer of the linear and angular momenta of photons to the free carriers in the interior of the graphene sheet. The second one, however, cannot be attributed to any photoelectric effect in an ideal honeycomb lattice of graphene. This two-dimensional lattice possesses a center of space inversion and does not allow for an electric current at normal incidence of the radiation. Thus, the appearance of photocurrents at normal incidence is a clear manifestation of the symmetry reduction of the system. We suggest that these currents, both the helicity-sensitive and those generated by linearly polarized radiation, also observed in experiment, are caused by the edges of the real finite-size samples.

This paper is organized as follows. In Sec. II, a short overview of the experimental technique is given. The experimental results are summarized in Sec. III. In Sec. IV, we present a phenomenological description and a microscopic theory of the photon drag effect in graphene. In Sec. V, we develop a theory of the edge photogalvanic effect responsible for the observed current at normal incidence of the radiation.

## II. EXPERIMENT

The graphene samples were prepared from natural graphite using the mechanical exfoliation technique<sup>1</sup> on an oxidized silicon wafer. The oxide thickness of 300 nm allowed to locate graphene flakes in an optical microscope and to assess their thickness. We checked the reliability of this method using Raman spectroscopy and

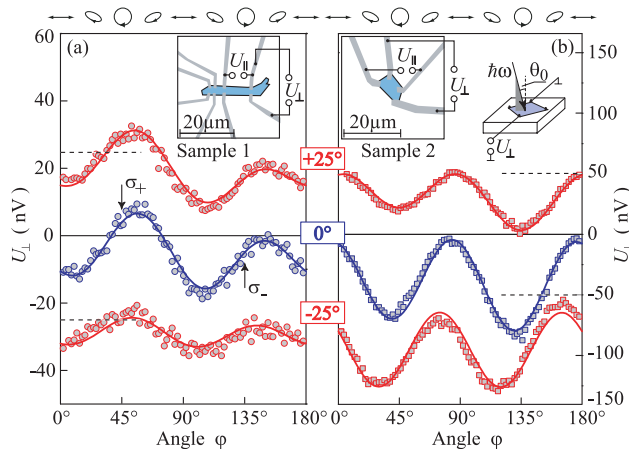


FIG. 1: Photosignals,  $U_{\perp}$ , in a single graphene sheet as a function of the angle  $\varphi$ , which determines the radiation helicity. The data are obtained at room temperature for various angles of incidence,  $\theta_0$ . The signal is measured nearly perpendicular to the light propagation direction applying radiation of the *cw* THz laser with the photon energy 10.5 meV, power  $\approx 20$  mW and a diameter of the laser spot about 1 mm. The data for  $\theta_0 = \pm 25^\circ$  are shifted by  $\pm 25$  nV [sample 1, panel (a)] and  $\pm 50$  nV [sample 2, panel (b)], respectively. The horizontal dashed lines show  $x$ -axes corresponding to  $U_{\perp} = 0$  for the shifted data. Full lines are fits to Eq. (1). We note that these fits can be obtained from superposition of the photon drag effect at oblique incidence [see Eqs. (12), (13)] and the photogalvanic effect at normal incidence [see Eq. (43)]. The insets show the sample geometry and experimental configuration. The ellipses on top illustrate the states of polarization for various angles  $\varphi$ .

low-temperature quantum Hall measurements on similar samples<sup>28</sup>. Typically samples were *p*-doped by adsorbed contaminants in the range of  $n \leq 2 \times 10^{12} \text{ cm}^{-2}$ . The Fermi energies were  $E_F \leq 165$  meV and the mobilities at room temperature of the order of  $2.5 \times 10^3 \text{ cm}^2/\text{Vs}$ . The flakes included in this study were all single layer. After recording the position of the flakes with respect to predefined markers, we contacted them with electron beam lithography and thermal evaporation of 60 nm Pd electrodes. The resistance of graphene measured between various contacts was in the range of 1 k $\Omega$ . Some flakes were cut into shape using oxygen based reactive ion etching. Insets in Figs. 1 and 2 show the shapes and the contact geometry of the four investigated samples indicated by the numbers 1, 2, 3 and 4. The samples were glued onto holders with conductive epoxy enabling the use of the highly doped silicon wafer as a back gate. The sample morphology was characterized by atomic force microscopy measurements under ambient conditions with the microscope in intermittent contact mode with standard silicon tips<sup>29</sup>.

The photocurrents were generated at room temperature applying THz radiation of an optically pumped continuous-wave (*cw*) CH<sub>3</sub>OH laser<sup>16</sup> operating at a wavelength  $\lambda = 118 \mu\text{m}$  (or the corresponding photon en-

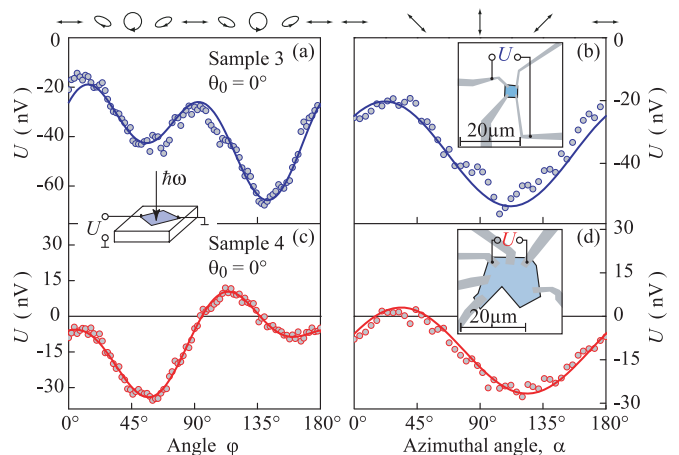


FIG. 2: Polarization dependences of the photoresponse obtained at normal incidence of the *cw* THz laser radiation for the samples 3 and 4. The two left panels show signals as a function of the radiation helicity, given by  $\varphi$ , and the two right panels as a function of the electric field orientation given by azimuthal angle  $\alpha$ . Full lines are fits to Eq. (1) [panels (a) and (c)] and Eq. (2) [panels (b) and (d)]. These fits can be obtained by the photogalvanic effect at normal incidence [see Eq. (43)]. The insets show the experimental arrangement and the samples geometry. The symbols on top of the left and right panels illustrate the states of polarization for various angles  $\varphi$  and  $\alpha$ , respectively.

ergy 10.5 meV) with the power  $P \approx 20$  mW and a diameter of the laser spot of about 1 mm. The radiation was modulated at chopper frequencies in the range from 120 to 600 Hz. The sign of the signal is defined as a relative phase with respect to the lock-in reference signal frequency, which was kept the same for all measurements. Additionally we used a high power pulsed NH<sub>3</sub> laser operating at  $\lambda = 148 \mu\text{m}$  and  $P \approx 30$  kW<sup>16</sup>. The photocurrent induced by the *cw* laser is measured across a 10 M $\Omega$  load resistor and recorded with lock-in technique. The signal magnitudes of Figs. 1-3 are given before amplification. The photoresponse to pulsed radiation is measured across a 50  $\Omega$  resistor.

The samples were excited both at normal and oblique incidence. In the case of oblique excitation, the angle  $\theta_0$  between the light propagation direction and the sample normal was varied from  $-25^\circ$  to  $+25^\circ$ . The experimental geometries are illustrated in the insets in Figs. 1 and 2 for oblique and normal incidence, respectively. In order to vary the radiation helicity we used a  $\lambda/4$  plate. The rotation of the plate resulted in the change of the degree of circular polarization after  $P_{\text{circ}} = \sin 2\varphi$ , where  $\varphi$  is the angle between the initial polarization vector of the laser light  $\mathbf{E}$  and the *c*-axis of the plate. The light polarization states for certain characteristic angles  $\varphi$  are sketched on top of Figs. 1 and 2. In some experiments we also used linearly polarized radiation. In this case the plane of polarization of the radiation was rotated by  $\lambda/2$  plates. This enabled us to vary the azimuthal an-

gle  $\alpha$  from  $0^\circ$  to  $180^\circ$  covering all possible orientations of the electric field vector in the graphene plane. The relative positions of the light polarization with respect to the graphene sample edges and contacts are shown on the top of Fig. 2(b).

### III. EXPERIMENTAL RESULTS

Irradiating graphene samples at normal as well as at oblique incidence we observed photocurrents in all investigated samples. The signal was detected at room temperature for both low power excitation level of  $cw$  laser and high power pulsed laser. In the latter case the width of the photocurrent pulses was about 100 ns, which corresponds to the THz laser pulse duration. In order to prove that the signal stems from the graphene flakes and not, e.g., from the substrate, we removed the graphene layer from one of the samples and observed that the signal disappeared.

Figure 1 shows the photoresponse  $U_\perp$ , which is proportional to the photocurrent  $j$ , of two samples 1 and 2 as a function of the angle  $\varphi$ , assigning the helicity. The signals are measured at different angles of incidence  $\theta_0 = 0, \pm 25^\circ$ . While the figure shows the photoresponse obtained from the pairs of contacts oriented almost perpendicular to the light propagation plane, a photocurrent has also been observed at any other pair of contacts. Generally, the helicity dependence of the photocurrent can be well fitted by

$$J = A \sin 2\varphi + B \sin 4\varphi + C \cos 4\varphi + D, \quad (1)$$

where  $A$ ,  $B$ ,  $C$  and  $D$  are fitting parameters. Such behavior, phenomenologically well described by symmetry arguments (see below), was found in all graphene samples. The fits to experimental data shown by solid lines in Fig. 1 demonstrate a good agreement. The first term on the right hand-side of Eq. (1), which is proportional to  $\sin 2\varphi$  and described by the parameter  $A$ , changes its sign upon reversing the photon helicity (marked by arrows). The analysis of the experimental data gives an evidence that a substantial contribution to the total photocurrent changes its sign upon switching the radiation helicity from right- ( $\sigma_+$ ) to left-handed ( $\sigma_-$ ) circularly polarized light, i.e., for the angles  $\varphi = 45^\circ$  and  $\varphi = 135^\circ$ , respectively. This is most spectacularly seen in the data obtained on sample 1, where the changing sign of the current is directly detected at normal incidence,  $\theta_0 = 0^\circ$  (Fig. 1a). The helicity driven photocurrent gives a substantial contribution to the photoresponse of two other samples as demonstrated in Figs. 2(a) and (c) for normal incidence of radiation.

A deeper insight into the photon-helicity driven photocurrents is given by their dependences on the incidence angle  $\theta_0$  presented in Fig. 3 for the samples 1 and 2. We obtained that the photoresponse of the helicity driven electric current is substantially different for the geometries, where the photocurrent is measured in the

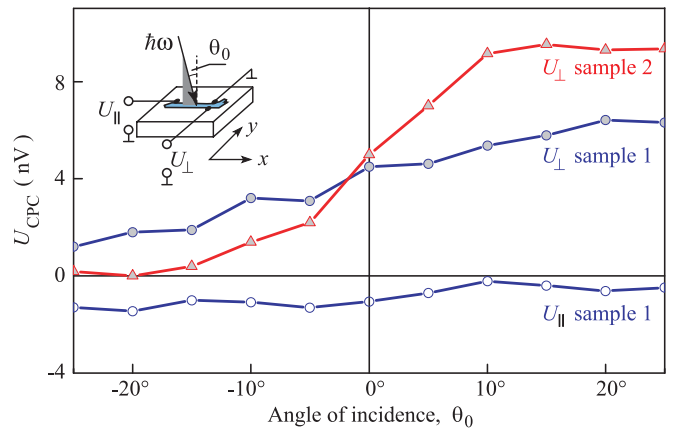


FIG. 3: Signals due to circularly polarized radiation  $U_{CPC} = [U(\varphi = 45^\circ) - U(\varphi = 135^\circ)]/2$  measured as a function of the incidence angle  $\theta_0$  in response to the  $cw$  THz laser radiation. Triangles and full circles show the transversal response,  $U_\perp$ , for samples 1 and 2, respectively. Open circles show the signal obtained in the longitudinal geometry,  $U_\parallel$ , for sample 2. The inset illustrates the experimental configuration.

direction transversal and almost longitudinal to the light propagation<sup>30</sup>. While the photocurrent measured in the longitudinal geometry is almost independent on the angle of incidence and reflects the signals obtained at normal incidence, in the transverse geometry it shows a superposition of two contributions being even and odd in the incidence angle. An important feature of the latter contribution is that its direction is determined by the light propagation plane, the radiation helicity and the sign of  $\theta_0$ , irrespective to the orientation of the sample edges by contrast to the photocurrents being even functions of the angle  $\theta_0$ .

Now we turn to the photocurrent contributions proportional to the coefficients  $B$  and  $C$  in Eq. (1). This photocurrent, in fact, does not require the radiation helicity and reflects the linear polarization component of the incident radiation. This has been checked in an independent experiment. By rotating now a  $\lambda/2$  plate we varied the relative position between the plane of the radiation polarization and the axes of the samples characterized by the azimuthal angle  $\alpha$ . The data are shown in Figs. 2(b) and (d) and can be well described in agreement with Eq. (1) by

$$J = 2B \sin 2\alpha + 2C \cos 2\alpha + D - C. \quad (2)$$

Corresponding fits are plotted by the solid lines in Figs. 2(b) and (d). Such a behavior of the photocurrent clearly demonstrates the linear-polarization sensitivity of the effects. Note that the difference  $D - C$  actually constitutes the polarization independent effect, which can be related to e.g. contacts and is outside of the scope of the present paper. Studying the dependence of the photocurrent on the angle of incidence for linearly polarized excitation we observed that, in contrast to the excitation with circularly polarized light, the measured photocur-

rents both in longitudinal and transverse geometries always result from the superposition of the contribution weakly dependent on  $\theta_0$ , which stems from normal incidence, and the one being odd in the angle  $\theta_0$  (not shown). Moreover, these contributions odd in  $\theta_0$  are interconnected: While the longitudinal one behaves as  $\cos 2\alpha$ , the transverse component is proportional to  $\sin 2\alpha$ .

To summarize, we observed that both the helicity dependent and helicity independent photocurrents have two contributions: (i) an even function of the incidence angle  $\theta_0$ , which dominates the signal at normal incidence, and (ii) a odd in the incidence angle contribution, which appears at oblique incidence only. Below in Sec. IV we demonstrate that the contributions to the photocurrent odd in the angle  $\theta_0$ , both circular and linear, stem from the interior of graphene and are caused by the photon drag effect, where the transfer of the momentum of the photons results in a directed motion of electrons. We present the phenomenological approach, which is based on symmetry arguments and is free from details of the microscopic model, and then the microscopic theory is put forward. The photoresponse at normal incidence, by contrast, can not be related with an ideal bulk material. In Sec. V, we show that these effects are due to the sample edges and give the corresponding microscopic theory.

## IV. THEORY OF PHOTON DRAG

### A. Photocurrents as a second-order response to the electromagnetic fields

In general, the photocurrents under study can be regarded as a second-order nonlinear steady-state response

$$j_\lambda^{(2)}(0,0) = \sigma_{\lambda\nu\eta}^{(2)}(\omega, \mathbf{q}) E_\nu(\mathbf{q}, \omega) E_\eta^*(\mathbf{q}, \omega) \quad (3)$$

to the electric field of a plane electromagnetic wave

$$\mathbf{E}(\mathbf{r}, t) = \mathbf{E}(\mathbf{q}, \omega) e^{-i\omega t + i\mathbf{q}\mathbf{r}} + \mathbf{E}^*(\mathbf{q}, \omega) e^{i\omega t - i\mathbf{q}\mathbf{r}}. \quad (4)$$

Here  $\mathbf{E}(\omega, \mathbf{q})$  is the complex electric-field amplitude with the frequency  $\omega$  and the wave vector  $\mathbf{q}$ ,  $\mathbf{j}^{(2)}(0,0)$  is the photocurrent density, zeros  $(0,0)$  indicate that we consider an electric current averaged in time and space. In a two-dimensional system the index  $\lambda$  runs only over the two in-plane coordinates  $x$  and  $y$  while the indices  $\nu$  and  $\eta$  can include the normal coordinate  $z$ . The second-order conductivity  $\sigma^{(2)}(\omega, \mathbf{q})$  can be expanded in powers of  $\mathbf{q}$ , hereafter we retain only the first two terms

$$\sigma_{\lambda\nu\eta}^{(2)}(\omega, \mathbf{q}) = \sigma_{\lambda\nu\eta}^{(2)}(\omega, 0) + \Phi_{\lambda\mu\nu\eta}(\omega) q_\mu. \quad (5)$$

The tensor  $\sigma_{\lambda\nu\eta}^{(2)}(\omega, 0)$  requires a lack of the inversion center in the symmetry point group of the system, it can conveniently be decomposed into two tensors  $\sigma^{(2,\pm)}$  symmetrical and antisymmetrical with respect to the index interchange  $\nu \leftrightarrow \eta$ . The symmetrical tensor  $\sigma_{\lambda\nu\eta}^{(2,+)}$

describes the linear photogalvanic effect (PGE). The antisymmetric tensor  $\sigma_{\lambda\nu\eta}^{(2,-)}$  is dual to a pseudotensor  $\gamma_{\lambda\xi}$  describing the circular PGE<sup>15–17,31</sup>. The contributions described by the fourth-rank tensor  $\Phi$  are allowed both in centrosymmetric and noncentrosymmetric media. In a simplified qualitative picture the linear- $\mathbf{q}$  contribution in Eq. (5) arises due to transfer of momenta from photons to free carriers and, therefore, is called the photon drag effect.

The photon-drag current can equivalently be presented in terms of spatial derivatives of the electric field  $\mathbf{E}(\mathbf{r}, \omega)$  as follows

$$j_\lambda^{(\text{drag})} = \Phi_{\lambda\mu\nu\eta}(\omega) \times \frac{i}{2} \left[ E_\nu(\mathbf{r}, \omega) \frac{\partial E_\eta^*(\mathbf{r}, \omega)}{\partial x_\mu} - E_\eta^*(\mathbf{r}, \omega) \frac{\partial E_\nu(\mathbf{r}, \omega)}{\partial x_\mu} \right]. \quad (6)$$

For the plane wave (4) the bilinear expression in the square brackets is independent of  $\mathbf{r}$ . Equation (6) permits one to make sure that the tensor  $\Phi_{\lambda\mu\nu\eta}$  in Eq. (5) describes the drag current even in case of the sample dimension  $L$  being smaller than the light wavelength provided  $L$  by far exceeds the carrier free path length  $l$ .

Similarly to the second-harmonic generation linear in the light wave vector, there are two mechanisms of the photon drag effect. The linear- $\mathbf{q}$  terms can appear in Eq. (5) either due to the gradient of electric field ( $qE^2$ -mechanism) or due to a combined action of the electric and magnetic field of the electromagnetic wave ( $EB$ -mechanism or the high-frequency Hall effect). In some sense, these mechanisms are analogues, respectively, of the magnetic-dipole and electric-quadrupole contributions to second-harmonic generation described by the difference  $\mathbf{j}^{(2)}(2\omega, 2\mathbf{q}) - \mathbf{j}^{(2)}(2\omega, 0)$ .

### B. Phenomenological description of the drag current in graphene

The ideal honeycomb lattice of graphene is described by the point group  $D_{6h}$ . The group contains the space inversion and, therefore, allows the photon-drag currents only because the circular and linear PGE are excluded by symmetry arguments<sup>15</sup>. Decomposing the tensor  $\Phi_{\lambda\mu\nu\eta}$  into symmetrical and antisymmetrical parts concerning the indices  $\nu$  and  $\eta$  the drag current can be written phenomenologically also as

$$j_\lambda = T_{\lambda\mu\nu\eta} q_\mu \frac{e_\nu e_\eta^* + e_\nu^* e_\eta}{2} I + \tilde{T}_{\lambda\mu\nu} q_\mu P_{\text{circ}} \hat{e}_\nu I. \quad (7)$$

Here  $I$  is the light intensity (energy flux through unit surface) related with the electric field by  $|\mathbf{E}(\mathbf{q}, \omega)|^2 = (2\pi/cn_\omega)I$ ,  $n_\omega$  is the refractive index at the frequency  $\omega$ ,

$$T_{\lambda\mu\nu\eta} = \frac{\pi}{cn_\omega} (\Phi_{\lambda\mu\nu\eta} + \Phi_{\lambda\mu\eta\nu}),$$

$$\tilde{T}_{\lambda\mu\xi} = -\frac{i\pi}{2cn_\omega} \sum_{\nu\eta} e_{\xi\nu\eta} (\Phi_{\lambda\mu\nu\eta} - \Phi_{\lambda\mu\eta\nu}),$$

$e_{\xi\nu\eta}$  is the unit antisymmetric tensor,  $\mathbf{j}$  is the current density,  $\mathbf{e}$  is the unit polarization vector of the electromagnetic wave,  $\hat{\mathbf{e}}$  is the unit vector pointing in the light propagation direction,  $P_{\text{circ}}$  is circular polarization degree related to the vectors  $\mathbf{e}$  and  $\hat{\mathbf{e}}$  by  $P_{\text{circ}}\hat{\mathbf{e}} = i(\mathbf{e} \times \mathbf{e}^*)$ .

The fourth-rank tensor  $T_{\lambda\mu\nu\eta}$  describes the linear photon drag effect which is insensitive to the sign of circular polarization and reaches its maximum for linearly polarized light, while the third rank pseudotensor  $\tilde{T}_{\lambda\mu\nu}$  stands for the circular photon drag current which changes its sign upon the reversal of photon helicity.

The symmetry analysis shows that, in the  $D_{6h}$  point group, the tensor  $T_{\lambda\mu\nu\eta}$  has four linearly independent components:  $T_1 = T_{xxxx} + T_{xyxy}$ ,  $T_2 = T_{xxxx} - T_{xyxy} = 2T_{xyxy}$ ,  $T_3 = 2T_{xzzx}$  and  $T_4 = T_{xxzz}$ . Then the first term in the right-hand side of Eq. (7) is reduced to

$$j_x = T_1 q_x \frac{|e_x|^2 + |e_y|^2}{2} I + T_2 \left( q_x \frac{|e_x|^2 - |e_y|^2}{2} + q_y \frac{e_x e_y^* + e_x^* e_y}{2} \right) I + T_3 q_z \frac{e_x e_z^* + e_x^* e_z}{2} I + T_4 q_x |e_z|^2 I, \quad (8a)$$

$$j_y = T_1 q_y \frac{|e_x|^2 + |e_y|^2}{2} I + T_2 \left( q_y \frac{|e_y|^2 - |e_x|^2}{2} + q_x \frac{e_x e_y^* + e_x^* e_y}{2} \right) I + T_3 q_z \frac{e_y e_z^* + e_y^* e_z}{2} I + T_4 q_y |e_z|^2 I, \quad (8b)$$

where  $x$  and  $y$  are the axes in the graphene plane, and  $z$  is the structure normal. Equations (8) clearly show that the photon drag current can be induced only at oblique incidence of the radiation and vanishes under normal incidence when both the in-plane component of the photon wave vector  $\mathbf{q}$  and the out-of-plane component of the polarization vector  $\mathbf{e}$  are zeros. The photocurrent contains both the longitudinal component induced in the incidence plane and determined by the parameters  $T_1, T_2, T_4$  and the transversal component proportional to  $T_2$ . The current described by the parameter  $T_3$  requires  $z$ -component of the photon wave vector.

For an elliptically polarized radiation, in particular, for circular polarization, the photon drag current in structures of the  $D_{6h}$  symmetry contains additional contributions proportional to components of the  $\tilde{T}_{\lambda\mu\xi}$  tensor:

$$j_x = \tilde{T}_1 q_y P_{\text{circ}} \hat{e}_z I - \tilde{T}_2 q_z P_{\text{circ}} \hat{e}_y I, \quad (9a)$$

$$j_y = -\tilde{T}_1 q_x P_{\text{circ}} \hat{e}_z I + \tilde{T}_2 q_z P_{\text{circ}} \hat{e}_x I, \quad (9b)$$

and sensitive to the radiation helicity. Here,  $\tilde{T}_1 = \tilde{T}_{xyz}$  and  $\tilde{T}_2 = \tilde{T}_{yzx}$  are linearly independent parameters. Similarly to the linear photon drag effect, the circular photocurrent (9) can be induced at oblique incidence only.

However, in contrast to the former, the circular photocurrent always flows perpendicularly to the light incidence plane.

It follows from very general considerations that, in two-dimensional systems, the contributions from  $T_3, T_4$  and  $\tilde{T}_2$  are small and unlikely to be observable. Indeed, in terms of the semiclassical Boltzmann equation the two-dimensional carriers are unaffected by the normal component of the electric field  $E_z$ , provided that the graphene layer is flat, and the terms in Eqs. (8), (9) proportional to  $e_z, e_z^*$  or  $|e_z|^2$  vanish. For interband quantum optical transitions, the photocurrent governed by the component  $q_z$  related to the currents  $\propto q_{x,y}$  has a small parameter  $ka$ , where  $k$  is the electron wave vector referred to the band extremum point and  $a$  is the well thickness in the semiconductor quantum wells or the carbon atom radius in the case of graphene. For intraband indirect optical absorption involving virtual transitions via other bands the parameter  $ka$  is multiplied by another small parameter  $\hbar\omega/\Delta$ , where  $\Delta$  is the energy distance to other bands. In graphene  $\Delta$  is the energy difference between the  $\pi$  and  $\sigma$  orbitals and has an order of several electronvolts.<sup>32</sup> Therefore, in the following we will ignore the  $T_3, T_4$  and  $\tilde{T}_2$  terms in Eqs. (8), (9).

Most studies on photon drag effect have been carried out in crystals with cubic symmetry<sup>33-38</sup>, simple metals<sup>39</sup> and in atomic gases<sup>40,41</sup>. In these systems the circular photon drag is forbidden because the symmetry equalizes the coefficients  $\tilde{T}_1$  and  $\tilde{T}_2$  in Eq. (9) so that the photocurrent  $\mathbf{j}$  becomes proportional to the vector product  $\mathbf{q} \times \hat{\mathbf{e}} = 0$ . In systems of uniaxial symmetry, anisotropic crystals, quantum-well structures, superlattices etc., the coefficients  $\tilde{T}_1$  and  $\tilde{T}_2$  are linearly independent and allow the circular drag photocurrent. Even more so, this effect is allowed in graphene where, as mentioned above, the coefficient  $\tilde{T}_2$  is negligible. It is worth mentioning that the appearance of the transverse linear photon drag effect in the vicinity of the metal surface was discussed in Refs. 42,43.

Figure 4 schematically illustrates the relative orientation of all remaining contributions in respect to the light propagation direction and its polarization state. This figure being in correspondence to Eq. (9) shows that the helicity driven photocurrent appears at oblique incidence only and flows perpendicularly to the light propagation direction, see Fig. 4(a). Furthermore it changes its sign upon reversal of the incidence angle. This is in full agreement with the experiment, see Fig. 3, where the odd contribution to the circular photocurrent is indeed observed for the transverse geometry only. By contrast, the linear photon drag effect is generated in both longitudinal [see Fig. 4(b)] and transversal geometries [see Fig. 4(c)] being also in agreement with the experimental findings.

Also, the polarization dependences given by Eqs. (8), (9) are observed experimentally. In order to simplify the comparison with the experiment we rewrite Eqs. (8) and (9) for the geometry relevant to the experiment with the light incidence plane being  $(xz)$  and the polarization

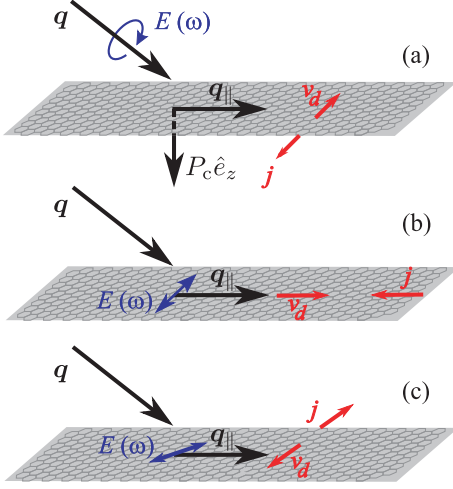


FIG. 4: Schematic illustration of the photon drag effects. Panel (a): circular photon drag effect, where the current is generated transverse to the light incidence plane (see Eqs. (9)). Panels (b) and (c): linear photon drag effect. Here both longitudinal and transverse current can be generated [see Eqs. (8)].

state of the light described by the angle  $\varphi$  for elliptically polarized light (in particularly, circularly polarized light) and the angle  $\alpha$  for linearly polarized light. In the first case one obtains

$$j_x(\varphi, \theta_0) \propto \frac{T_1 \sin \theta_0}{4} [4 \cos^2 \theta_0 + \sin^2 \theta_0 (1 - \cos 4\varphi)] \\ + \frac{T_2 \sin \theta_0}{4} [4 \cos^2 \theta_0 + (1 + \cos^2 \theta_0)(\cos 4\varphi - 1)]$$

$$j_y(\varphi, \theta_0) \propto \tilde{T}_1 \sin \theta_0 \cos \theta_0 \sin 2\varphi + \frac{T_2}{2} \sin \theta_0 \cos \theta_0 \sin 4\varphi, \quad (10)$$

while in the second case one has

$$j_x(\alpha, \theta_0) \propto T_1 \sin \theta_0 (1 - \sin^2 \theta_0 \cos^2 \alpha) \\ + T_2 \sin \theta_0 (\cos 2\alpha - \cos^2 \alpha \sin^2 \theta_0) \\ j_y(\alpha, \theta_0) \propto \sin \theta_0 \cos \theta_0 T_2 \sin 2\alpha. \quad (11)$$

For the small incidence angles as in our experiment one retains only linear in  $\theta_0$  terms and obtains from Eqs. (10), (11) the following simplified relations describing the photocurrent dependences on  $\varphi$ :

$$j_x(\varphi, \theta_0) \propto T_1 \sin \theta_0 + \frac{T_2 \sin \theta_0}{2} (\cos 4\varphi + 1) \\ j_y(\varphi, \theta_0) \propto \tilde{T}_1 \sin \theta_0 \sin 2\varphi + \frac{T_2}{2} \sin \theta_0 \sin 4\varphi, \quad (12)$$

and  $\alpha$ :

$$j_x(\alpha, \theta_0) \propto T_1 \sin \theta_0 + T_2 \sin \theta_0 \cos 2\alpha \\ j_y(\alpha, \theta_0) \propto \sin \theta_0 \cos \theta_0 T_2 \sin 2\alpha. \quad (13)$$

The dependence of the experimentally observed photocurrents odd in the angle incidence on the parameters  $\alpha$  and  $\varphi$  characterizing the polarization states of the radiation is in agreement with Eq. (12) and (13). Indeed, as it is seen from Fig. 1 (also from Fig. 3) the odd in  $\theta_0$  contribution to helicity driven photocurrent,  $\propto \sin 2\varphi$ , is observed only in the transversal with respect to the light incidence plane geometry. By contrast, the contribution to the current odd in the incidence angle, which was measured in the longitudinal geometry, is described by  $\cos 4\varphi$  or  $\cos 2\alpha$  (not shown) demonstrating the linear photon drag effect.

It is worth mentioning that the coefficients describing the linear and circular drag effects have different properties under time reversal,  $t \rightarrow -t$ . Namely, the circular polarization sign changes at time reversal while the linear polarization sign remains. Both the electric current and the photon wave vector are odd functions with respect to the replacement  $t \rightarrow -t$ , therefore the constants  $\tilde{T}_1$  and  $\tilde{T}_2$  are proportional to an odd number of dissipative parameters and the constants  $T_i$  ( $i = 1, \dots, 4$ ) to an even number of dissipative parameters.

The above analysis, which yields a good agreement with the experiment, was performed using the ideal symmetry for the graphene layer characterized by the point group  $D_{6h}$ . The real structures, however, are deposited on a substrate, which removes the equivalence of the  $z$  and  $-z$  directions and reduces the symmetry to the  $C_{6v}$  point group. Our analysis demonstrates that the photon drag effect does not change qualitatively with the reduction of symmetry and only the values of the parameters  $T_1, \dots, T_4, \tilde{T}_1$ , and  $\tilde{T}_2$  may change. However, now the system lacks an inversion center, and photogalvanic effects become possible. The photogalvanic contributions to the total electric current are phenomenologically given by

$$j_\lambda = \chi_{\lambda\mu\nu} \frac{e_\mu e_\nu^* + e_\mu^* e_\nu}{2} I + \gamma_{\lambda\mu} P_{circ} \hat{e}_\mu I. \quad (14)$$

In structures of the  $C_{6v}$  point group, non-zero components of the tensors  $\chi_{\lambda\mu\nu}$  and  $\gamma_{\lambda\mu}$  describing the linear and circular photogalvanic effects, respectively, are  $\chi_{xxx} = \chi_{yyy}$  and  $\gamma_{xy} = -\gamma_{yx}$ . It means that the linear photogalvanic effect requires a  $z$ -component of the electric field. Moreover, the circular photogalvanic effect also needs this component because, e.g.,  $\hat{e}_x \sim i(e_x e_z^* - e_z e_x^*)$  vanishes if the  $z$  component of the field is absent. These requirements result in vanishingly small contribution of the photogalvanic effects to the total electric current, similar to the arguments, which exclude photon drag effect components given by the constants  $T_3, T_4$  and  $\tilde{T}_2$ .

To summarize, the analysis of the photocurrents odd-in  $\theta_0$  can be reduced to the photon drag effects solely, and can be applied to the experimental data independent of the influence of the substrate indicated above for the symmetry of the graphene flakes.

### C. Microscopic theory

Now we turn to the microscopic theory of both linear and circular photon drag effect. In the following we focus on the classical regime of interaction between the radiation and the electron ensemble in graphene which is realized as soon as  $\hbar\omega \ll \mathcal{E}$ , where  $\mathcal{E}$  is the characteristic electron energy, the Fermi energy in the degenerate electron gas or thermal energy  $k_B T$  for non-degenerate electrons ( $k_B$  is the Boltzmann constant). In this case only intraband transitions are involved. This approach is similar to the classical consideration of the drag effect in semiconductors<sup>33–37</sup>. The theory for the drag effect in the quantum range of frequencies,  $\hbar\omega \sim \mathcal{E}$  or higher, involving both interband and intraband optical transitions is out of scope of this paper and will be presented elsewhere [44].

#### 1. Qualitative picture

First we present a qualitative microscopic picture of the drag effect exclusively based on Newton's second law of motion

$$\frac{d\mathbf{p}}{dt} + \frac{\mathbf{p}}{\tau} = e\mathbf{E}(\mathbf{r}, t) + \frac{e}{c}[\mathbf{v} \times \mathbf{B}(\mathbf{r}, t)], \quad (15)$$

where  $e = -|e|$  is the electron charge,  $\mathbf{p}$  and  $\mathbf{v}$  are the electron momentum and velocity,  $\mathbf{p}/\tau$  is the friction force due to electron scattering with  $\tau$  being the scattering time. Assuming for simplicity the propagation of linearly-polarized radiation along the graphene (grazing incidence) with in-plane wave vector and electric field and out-of-plane magnetic field:  $\mathbf{q} \parallel x$ ,  $\mathbf{E} \parallel y$ ,  $\mathbf{B} \parallel z$ , as shown in Fig. 5. The generation of a *dc* current can be described in the framework of the high-frequency Hall effect<sup>33</sup>. It is seen from Fig. 5(a) that during the first half of the period  $T_\omega = 2\pi/\omega$  of the electro-magnetic field oscillation where the both field components  $E_y$  and  $B_z$  are positive the electron is exposed to action of the two forces  $F_y = eE_y$  and  $F_x = ev_y B_z$  like in the Hall effect. In the absence of friction the phase shift between oscillations of the velocity  $v_y$  and the field  $B_z$  equals  $90^\circ$  and the average value of  $F_x$  vanishes. Allowance for the friction results in a drift along the  $x$  axis. In the second half-period  $T_\omega/2$  both fields  $E_y$  and  $B_z$  simultaneously reverse and the drift velocity retains its direction. As a result, a non-vanishing time-averaged drag current is induced in the direction of  $\mathbf{q}$ . Obviously, the reversal  $\mathbf{q} \rightarrow -\mathbf{q}$  results in a change of relative sign of the electric- and magnetic-field components and, consequently, in the current reversal.

This is the well-known longitudinal linear photon drag effect. In graphene, as distinct from bulk cubic crystal, the photon-drag mechanism due to the high-frequency Hall effect has a characteristic polarization dependence, see Eqs. (8) for  $T_3 = T_4 = 0$ . Indeed, if the electric field of the grazing-incidence radiation is rotated around  $\mathbf{q}$  by an angle  $\alpha$ , then its in-plane component varies  $\propto \cos\alpha$ , the out-of-plane component of the magnetic field  $B_z$  behaves just as  $E_y$ , and the drag current  $j_x \propto e_y^2$  decreases by  $\cos^2\alpha = (1 + \cos 2\alpha)/2$ . The geometry of incidence in the plane  $(x, z)$  at arbitrary oblique angle  $\theta_0$  is analyzed in the same way. For the *s*-polarized light, the consideration is completely the same, a decrease of  $B_z$  by a factor of  $\sin\theta_0$  is automatically reproduced by the corresponding change of  $q_x = |\mathbf{q}|\sin\theta_0$ . For the linear polarization with the angle  $\alpha$  different from integer multiples of  $90^\circ$ , the both components  $E_x$  and  $E_y$  are non-zero which yields a  $y$ -component of the drag current proportional to  $\sin\theta_0 \sin 2\alpha$ .

For the *EB*-mechanism, we could ignore the spatial dependence of the electric and magnetic fields. While considering the  $qE^2$ -mechanism we can ignore the magnetic field in the right-hand side of Eq. (15) but take into account the first-order spatial correction and present the electric field of the linearly polarized light as

$$\mathbf{E}(\mathbf{r}, \omega) = 2\mathbf{E}_0[\cos(\omega t) - 2q_x x \sin(\omega t)], \quad (16)$$

where  $\mathbf{E}_0$  is the electric field amplitude assumed, without loss of generality, to be real. At the first step we find the linear response

$$\mathbf{p}(t) = e\tau\mathbf{E}_{0\parallel}\text{Re}\left(\frac{e^{-i\omega t}}{1 - i\omega\tau}\right) \quad (17)$$

and the corresponding velocity  $\mathbf{v}(t)$ , where  $\mathbf{E}_{0\parallel}$  is the in-plane component of the vector  $\mathbf{E}_0$ . At the next step we calculate the oscillation of the electron position  $x(t) = \int v_x(t)dt$ . Finally, the function  $x(t)$  is substituted into the second term of Eq. (16) and then the time-average of this term is taken. As a result we obtain an additional contribution  $\propto q_x E_0^2$  to the continuous force acting on the electron.

The circular photon drag effect<sup>23–25</sup> can be described in a similar way. However, in this case one should take into account in Eq. (15) not only the Lorentz force or the spatial gradient of the electric field but also the phase shift by  $90$  degrees of the two orthogonal oscillating electric-field components  $\mathbf{E}_1 \perp \mathbf{E}_2 \perp \mathbf{q}$ . Then one can show that, since the phase of the oscillation  $\mathbf{p}(t)$  is retarded in time by  $\arctan(\omega\tau)$  relative to  $\mathbf{E}(t)$ , see Eq. (17), the circularly polarized electromagnetic wave as well induces the drag current which is perpendicular to  $\mathbf{q}_{\parallel}$ . The sign reversal of radiation helicity means a change  $90^\circ \rightarrow -90^\circ$  of the phase shift between the  $\mathbf{E}_1$  and  $\mathbf{E}_2$  components and a reversal of the circular drag current.

The performed qualitative consideration clearly confirms the statement made in Sect. IV.A that the interpretation of photon drag current in study is independent

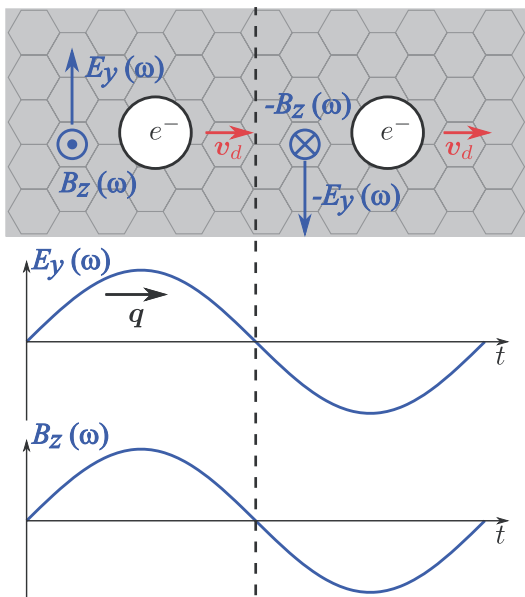


FIG. 5: Schematic illustration of the high-frequency Hall effect resulting in the photon drag effect.

of the relation between the sample linear in-plane dimension,  $L$ , and the light wave length  $\lambda$  but requires but requires a small ratio  $l/L$ , where  $l$  is the mean free path length  $v\tau$ , as well as a small product  $ql$ .

## 2. Boltzmann equation treatment

We develop a microscopic kinetic theory of the photon drag effect for the simplest model of the graphene band structure. We consider only the conduction and valence band states in the  $\mathbf{K}$  and  $\mathbf{K}'$  valleys formed from the  $\pi$ -orbitals of carbon atoms. In each valley, the effective Hamiltonian is a  $2 \times 2$  matrix

$$\mathcal{H} = \hbar v(\mathbf{k} \cdot \boldsymbol{\sigma}), \quad (18)$$

which describes both the conduction and valence bands of a graphene layer. Here  $v$  is the electron speed in graphene,  $\mathbf{k} = (k_x, k_y)$  is the two-dimensional wave vector referred to the Dirac point,  $\boldsymbol{\sigma}$  is a matrix two-dimensional vector with components  $\sigma_x$  and  $\sigma_y$  being the Pauli matrices in the pseudospin space.

In accordance with the definition (4) the electric and magnetic fields of the incident wave are taken in the form

$$\mathbf{E} = \mathbf{E}_0 e^{i(\mathbf{q}\mathbf{r} - \omega t)} + \text{c.c.}, \quad \mathbf{B} = \mathbf{B}_0 e^{i(\mathbf{q}\mathbf{r} - \omega t)} + \text{c.c.}, \quad (19)$$

where  $\mathbf{E}_0$  and  $\mathbf{B}_0$  are the complex amplitudes which are orthogonal to each other and to the wave vector  $\mathbf{q}$ . In the case of a linearly polarized light the vectors  $\mathbf{q}$ ,  $\mathbf{E}$  and  $\mathbf{B}$  form a right-hand triple. It is worth noting that the electric and magnetic fields acting on an electron in graphene lying on a substrate are different from those of an incident wave owing to the presence of substrate.

To be specific, let us assume that  $(xz)$  is the radiation incidence plane. Therefore,  $E_{0,y} = E_{0,y}^{(i)}(1 + r_s)$  and  $E_{0,x} = E_{0,x}^{(i)}(1 + r_p)$ , where the superscript  $(i)$  denotes the incident waves and  $r_s$ ,  $r_p$  are the amplitude reflection coefficients in the  $s$  and  $p$  polarizations, respectively. Similar relation holds for the  $z$ -component of the magnetic field,  $B_{0,z} = B_{0,z}^{(i)}(1 + r_s)$ . We expect that the metallic contacts attached to our small samples cause an inessential distortion of the plane-wave character of the electromagnetic field.

Following Ref. 34 the kinetic equation for the electron distribution function  $f(\mathbf{k}, \mathbf{r}, t)$  in a given valley reads

$$\frac{\partial f}{\partial t} + \mathbf{v} \frac{\partial f}{\partial \mathbf{r}} + \frac{e}{\hbar} \left( \mathbf{E} + \frac{1}{c} [\mathbf{v} \times \mathbf{B}] \right) \frac{\partial f}{\partial \mathbf{k}} = Q\{f\}. \quad (20)$$

Here  $c$  is the light speed in vacuum,  $\mathbf{v} = \mathbf{v}_{\mathbf{k}}$  is the electron velocity in the state with the wave vector  $\mathbf{k}$ ,

$$\mathbf{v}_{\mathbf{k}} = \frac{1}{\hbar} \frac{\partial \varepsilon_{\mathbf{k}}}{\partial \mathbf{k}} = v \frac{\mathbf{k}}{|\mathbf{k}|}, \quad (21)$$

$\varepsilon_{\mathbf{k}} = v\hbar k$  is the electron dispersion, and  $Q\{f\}$  is the collision integral.

The drag current is proportional to the light intensity and, therefore, appears in the second order in the electromagnetic fields. Correspondingly, we solve Eq. (20) by iterations with respect to the electric and magnetic fields and represent the electron distribution function as

$$f(\mathbf{k}, \mathbf{r}, t) = f_0(\varepsilon_{\mathbf{k}}) + \left[ f_1(\mathbf{k}) e^{i(\mathbf{q}\mathbf{r} - \omega t)} + \text{c.c.} \right] + f_2(\mathbf{k}) + \dots, \quad (22)$$

where  $f_0(\varepsilon_{\mathbf{k}})$  is the equilibrium distribution function,  $f_1(\mathbf{k})$  describes the linear response to the fields,  $f_2(\mathbf{k})$  is a homogeneous time-independent correction which appears in the second order in  $\mathbf{E}$ ,  $\mathbf{B}$ , and the omitted terms (...) describe other contributions including those oscillating with a double frequency and terms of the higher order in  $\mathbf{E}$ ,  $\mathbf{B}$ . The direct current caused by the photon drag effect is given by

$$\mathbf{j} = 4e \sum_{\mathbf{k}} \mathbf{v}_{\mathbf{k}} f_2(\mathbf{k}), \quad (23)$$

where the factor 4 accounts for the spin and valley degeneracy.

The first-order correction  $f_1(\mathbf{k})$  can be found by solving the linearized Eq. (20) with the result

$$f_1(\mathbf{k}) = -\frac{e\tau_1 E_0 f'_0}{1 - i\omega\tau_1} \times \left[ (\mathbf{e}\mathbf{v}) - i\tau_2 \frac{(\mathbf{q}\mathbf{v})(\mathbf{e}\mathbf{v}) - v^2(\mathbf{q}\mathbf{e})/2}{1 - i\omega\tau_2} + \frac{(\mathbf{q}\mathbf{e})v^2}{2\omega} \right]. \quad (24)$$

Here,  $f'_0 = df_0/d\varepsilon_{\mathbf{k}}$ ,  $\tau_1$  is the momentum relaxation time (more precisely, relaxation time of the first angular harmonic of the distribution function) and  $\tau_2$  is the relaxation time of the second angular harmonic. While deriving Eq. (24), we took into account that  $\tau_2 |\mathbf{q}|v, |\mathbf{q}|v/\omega \ll$



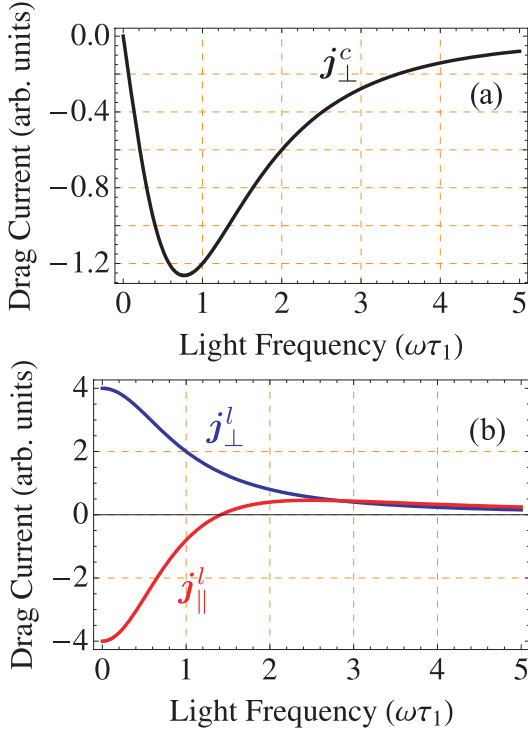


FIG. 6: Theoretical frequency dependences of (a) the circular photon-drag current,  $j_{\perp}^c$ , and (b) the linear photon-drag currents, both longitudinal ( $j_{\parallel}^l$ ) and transversal ( $j_{\perp}^l$ ), induced in bulk graphene sheet at oblique incidence and calculated after Eq. (26), (27). The drag current is given in arbitrary units and the frequency is presented in the dimensionless form as  $\omega\tau_1$ , where  $\tau_1$  is the momentum relaxation time.

1, in which case the second and third terms in the square brackets are small corrections to the first one. Moreover, the energy relaxation time  $\tau_e$  (relaxation time for the zeroth angular harmonics of the nonequilibrium distribution function) was assumed to be much longer than all other time scales in the system, namely,  $\tau_1, \tau_2, 1/\omega$ . The latter assumption allows us to neglect corrections to the distribution function related to energy relaxation processes and allow for this relaxation time to be infinite<sup>34</sup>. In this connection we note that the first term in Eq. (24) contains the first-order angular harmonics of the wave vector, the second term contains the second-order harmonics while the third term is angle independent.

The second-order correction  $f_2(\mathbf{k})$  averaged in time and space is found from the equation

$$\frac{2e}{\hbar} \text{Re} \left\{ \left( \mathbf{E}_0 + \frac{1}{c} [\mathbf{v} \times \mathbf{B}_0] \right) \frac{\partial f_1^*}{\partial \mathbf{k}} \right\} = Q \{ f_2 \}, \quad (25)$$

where the asterisk denotes the complex conjugation. There are two contributions to  $f_2(\mathbf{k})$  related to the above-mentioned  $EB$ - and  $qE^2$ -mechanisms: the first arises from a product of the Lorentz force and the main term in Eq. (24), and the second results from a product of the electric-field force and the  $\mathbf{q}$ -dependent terms in Eq. (24).

Substituting the solution of Eq. (25) into Eq. (23) we

arrive at the following expressions

$$T_1 = -\frac{4\pi e^3 v^4}{\omega c} \sum_{\mathbf{k}} \frac{\tau_1 f_0'}{1 + \omega^2 \tau_1^2} \times \left[ 2 \left( \frac{d\tau_1}{d\varepsilon_k} + \frac{\tau_1}{\varepsilon_k} \right) - \frac{1 - \omega^2 \tau_1 \tau_2}{1 + \omega^2 \tau_2^2} \left( \frac{d\tau_1}{d\varepsilon_k} - \frac{\tau_1}{\varepsilon_k} \right) \right], \quad (26a)$$

$$T_2 = -\frac{4\pi e^3 v^4}{\omega c} \sum_{\mathbf{k}} \frac{\tau_1 f_0'}{1 + \omega^2 \tau_1^2} \left( \frac{d\tau_1}{d\varepsilon_k} - \frac{\tau_1}{\varepsilon_k} \right) \quad (26b)$$

for the constants  $T_1$  and  $T_2$  describing the linear photon-drag current in the phenomenological equations (8). It is worth noting that in the low frequency limit,  $\omega\tau_1, \omega\tau_2 \ll 1$ , the coefficients  $T_1, T_2$  tend to infinity as  $\omega^{-1}$ . However the drag current has a finite limit at  $\omega \rightarrow 0$  since it is proportional to  $qT_{1,2}$  and  $q \propto \omega$ . It should also be pointed out that, according to the definition (19), the static fields  $E$  and  $B$  differ by factors of 2 from the amplitudes  $E_0$  and  $B_0$  of the corresponding fields taken at  $\omega \rightarrow 0$  and, therefore, the constant relating the current at  $\omega \rightarrow 0$  with the squared amplitude  $E_0^2$  and the constant relating the static Hall current with the product of static fields  $E$  and  $B$  differ by a factor of 4.

In the same way we derive the constant  $\tilde{T}_1$  describing in Eqs. (9) the circular photon-drag effect

$$\tilde{T}_1 = \frac{2\pi e^3 v^4}{c} \sum_{\mathbf{k}} \frac{\tau_1^2 (1 + \tau_2/\tau_1) f_0'}{[1 + (\omega\tau_1)^2][1 + (\omega\tau_2)^2]} \left( \frac{d\tau_1}{d\varepsilon_k} - \frac{\tau_1}{\varepsilon_k} \right). \quad (27)$$

It is finite at  $\omega \rightarrow 0$  which means the vanishing of the circular photocurrent in the static-field limit as expected because, for static fields, ellipticity is forbidden.

The time inversion symmetry imposes the certain restrictions on the coefficients in Eqs. (8) and (9): microscopic expressions for  $T_j$  ( $j = 1..4$ ) and  $\tilde{T}_j$  ( $j = 1, 2$ ) must be proportional, respectively, to even and odd number of dissipative constants, in our case the relaxation times  $\tau_1, \tau_2$  or the inverse times  $\tau_1^{-1}, \tau_2^{-1}$ . One can see that Eqs. (26) and (27) for the linear and circular drag effects satisfy these general rules.

Thus, we have derived microscopic expressions for the phenomenological constants in Eqs. (8a), (8b), Eqs. (9a) and (9b) which, as we addressed above, describe well all experimental findings. The developed microscopic theory yields all allowed contributions to the photon drag effect in the model where only  $\pi$ -orbitals of carbon atoms are taken into account.

Figure 6 shows calculated frequency dependences of the photocurrent. In the calculation we assume that the electron scattering in graphene is short-range, in which case one has  $\tau_1 = 2\tau_2 \propto \varepsilon_k^{-1}$ . It is seen that at small frequencies,  $\omega \rightarrow 0$ , the circular photon drag effect vanishes and the linear photocurrent reaches its maximum values. The absolute value of  $j^c$  has a maximum at  $\omega\tau_1 \approx 0.8$  and decreases as  $\omega^{-4}$  at high frequencies,  $\omega\tau_1, \omega\tau_2 \gg 1$ . The linear photon-drag current exhibits a decrease at high-frequency  $\propto \omega^{-3}$ .

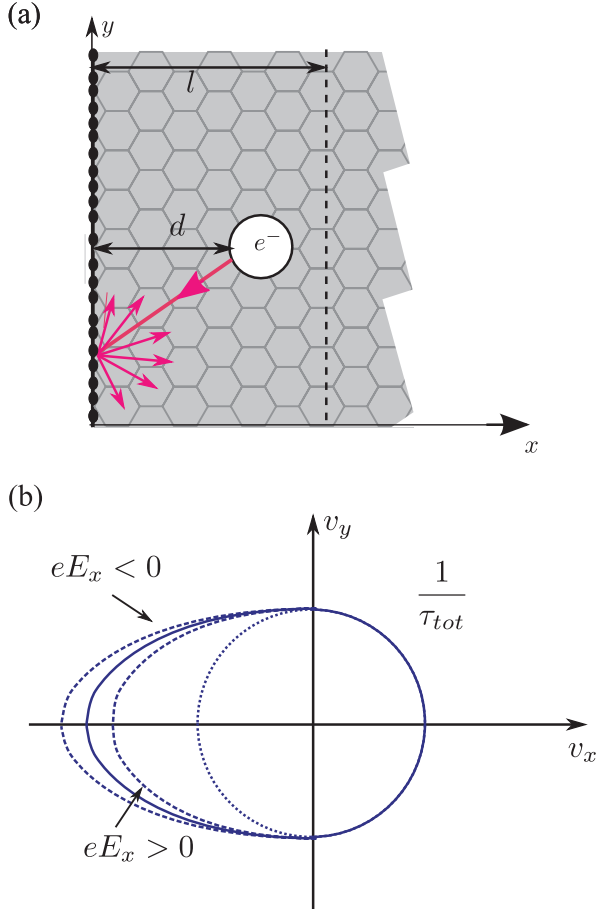


FIG. 7: Schematic illustration of the edge current generation in a sample of finite size.

Finally, we note that together with electrons in the conduction band, holes in the valence band also contribute to the photocurrent. The hole contribution to the current is obtained from Eqs. (26), (27) by the replacement  $e \rightarrow -e$  and the equilibrium electron distribution function  $f_0$  by the hole distribution  $f_0^{(\text{hole})}$ .

## V. EDGE PHOTOCURRENTS

Here we develop a theory of the photocurrent generation in graphene at normal incidence. In bulk graphene sheets of the  $D_{6h}$  or  $C_{6v}$  symmetry arguments the effect is forbidden. In order to explain its appearance in experiment, we need to take into account the graphene edges which locally reduce the symmetry<sup>45</sup>.

### A. Model

The existence of edge currents induced both by linearly or circularly polarized radiation can be understood in the framework of the model depicted in Fig. 7. We will show

that the current can be generated along the sample edge in a narrow channel of the width comparable to the mean free path  $l$ . Then, if the opposite sample edges, in the following the left and right edges, are non-equivalent, the edge currents do not compensate each other resulting in a non-zero net electric current. Otherwise, currents flowing along the opposite edges are oppositely directed and have the same absolute values. In the simplest model of the edge inequivalence, the electrons are specularly reflected from the right edge of the sample and diffusively scattered by the left one, as illustrated in Fig. 7. In a more general model, we can separate the edge reflectivity into two parts, specular  $R_{\text{sp}}$  and diffuse  $R_{\text{dif}}$ , satisfying the identity  $R_{\text{sp}} + R_{\text{dif}} = 1$ . In this model the net current is proportional to the difference  $R_{\text{dif},L} - R_{\text{dif},R}$  of the left- and right-edge diffusivenesses. For distinctness, we consider the current generation near the sample left edge and refer to Fig. 7. An important point to bear in mind is that an electron traveling in the  $l$ -thick stripe adjacent to the edge randomly changes its direction of motion along the  $y$  axis not only in the bulk scattering processes described by the relaxation time  $\tau_1$  but also in the diffusive reflection at the edge. Thus, its total scattering rate is a sum of two terms,

$$\frac{1}{\tau_{\text{tot}}} = \frac{1}{\tau} + R_{\text{dif},L} \frac{|v_x|}{d} \Theta(-v_x), \quad (28)$$

where  $d$  is the distance from the electron to the left edge, see Fig. 7, and  $\Theta(v)$  is the Heaviside function. The factor  $\Theta(-v_x)$  ensures that the additional contribution to  $\tau_{\text{tot}}^{-1}$  exists only for the carrier moving towards the edge. The dependence of the scattering time  $\tau_{\text{tot}}$  on the velocity direction is plotted in Fig. 7(b).

The  $x$ -component of electric field results in the oscillating correction to the electron velocity  $x$ -component:

$$v_x = v_x^0 + \delta v_x, \quad (29)$$

where

$$\delta v_x \sim \frac{e\tau E_x v}{(1 - i\omega\tau)p} e^{-i\omega t} + \text{c.c.}, \quad (30)$$

where  $p$  is the electron momentum corresponding to its mean kinetic energy. The modulation of the velocity results in the modulation of the scattering time  $\tau$  in agreement with Eq. (28), since electron reaches the boundary faster or slower depending on the value of  $eE_x$ , see Fig. 7(b).

The  $dc$  current along the edge is generated by  $y$  component of the field and, according to Drude theory, is proportional to the time-averaged product of  $E_y \tau_{\text{tot}}$ :

$$J_y \sim e^2 N l \frac{v}{p} \text{Re}\{\overline{E_y^* \delta \tau}\}. \quad (31)$$

Here  $N$  is the electron concentration,  $Nl$  is the electron density per unit length in the vicinity of the edge, overline means the averaging over time,

$$\delta \tau = \tau_{\text{tot}} - \tau \sim \Theta(v_x) \frac{\delta v_x}{l} \tau^2. \quad (32)$$

is the oscillating correction to the scattering time, and, for simplicity, we assumed that  $R_{\text{diff},L} \sim 1$ . The value and direction of the  $dc$  current is controlled by the relative phase of the  $E_y$  and  $\tau_{\text{tot}}$ , or accordingly  $v_x$  oscillations. At  $\omega\tau \ll 1$  the oscillations of  $E_x$  and  $v_x$  are in phase (no retardation) and the  $dc$  current appears at linear polarization of incident radiation where  $E_x$  and  $E_y$  components oscillate in phase. With an increase of  $\omega\tau$  the retardation effect comes into play and, in addition to the linear photocurrent, a helicity dependent response appears: the oscillations of  $\tau_{\text{tot}}$  appear to be phase-shifted with respect to the oscillations of  $E_x$  and for the circularly polarized wave where  $E_x$  and  $E_y$  are  $\pi/2$  phase-shifted the  $dc$  current is generated. Taking the average one can find that

$$\text{LPGE: } J_y^{\text{lin}} \sim \frac{e^3 v^2}{p^2} (E_x E_y^* + E_y E_x^*) \tau^3 N, \quad (33)$$

$$\text{CPGE: } J_y^{\text{circ}} \sim \omega\tau \frac{e^3 v^2}{p^2} i(E_x E_y^* - E_y E_x^*) \tau^3 N, \quad (34)$$

at  $\omega\tau \ll 1$ .<sup>46</sup> Superposition of these two current contribution yields polarization dependence of the photocurrent observed in experiment. Indeed, in the experimental geometry, where elliptically polarized radiation is obtained by rotation of the  $\lambda/4$  plate, polarization determined terms reduces to  $E_x E_y^* + E_y E_x^* = B \sin(4\varphi) + C \cos(4\varphi)$  and  $i(E_x E_y^* - E_y E_x^*) = A \sin 2\varphi$  being in agreement with experimental findings (see Fig. 1 and 2). Also in the set-up, where linear polarization is rotated by the angle  $\alpha$ , we obtain from Eq. (33)  $E_x E_y^* + E_y E_x^* = 2B \sin(2\alpha) + 2C \cos(2\alpha)$  which also agrees with experiment (see Fig. 2).

As we mentioned above, different edges of the sample make different contributions to the photocurrents. Consider the square-shaped sample and assume that all the sample edges scatter electrons diffusively. Obviously, the currents flowing along the opposite edges of the sample should have opposite directions. The current topology depends on the radiation polarization state. In accordance with our model, the helicity driven current should wind in the same direction, clock-wise or counter-clock-wise depending on the radiation helicity, for all the sample edges since the helicity,  $i(E_x E_y^* - E_y E_x^*)$  is preserved at the rotation by  $90^\circ$ . Hence, the distribution of helicity driven current should form a vertex, whose winding direction changes with the change of light helicity. However, it is not the case for the photocurrent caused by linearly polarized light and described by the combination  $E_x E_y^* + E_y E_x^*$ . The latter changes its sign at the  $90^\circ$  rotation, hence, the linear photocurrents flow towards (or outwards) the same corner for adjacent edges.

## B. Microscopic theory

The microscopic theory of this effect is developed in the framework of kinetic equations for the classical fre-

quency range. The equation for the distribution function  $f(\mathbf{k}, x, t)$  of electrons in the conduction band in a semi-infinite sample ( $x \geq 0$ ) has the form

$$\frac{\partial f}{\partial t} + v_x \frac{\partial f}{\partial x} + \frac{e\mathbf{E}(t)}{\hbar} \frac{\partial f}{\partial \mathbf{k}} = Q\{f\}, \quad (35)$$

where  $\mathbf{E}(t) = \mathbf{E}_0 e^{-i\omega t} + \mathbf{E}_0^* e^{+i\omega t}$  is the electric field of the radiation, which is assumed uniform in the graphene plane in the geometry of normal incidence. The distribution function can be expanded in series in the electric field as follows

$$f(\mathbf{k}, x, t) = f_0(\varepsilon_{\mathbf{k}}) + [f_1(\mathbf{k}, x) e^{-i\omega t} + \text{c.c.}] + f_2(\mathbf{k}, x) + \dots, \quad (36)$$

where  $f_0(\varepsilon_{\mathbf{k}})$  is the equilibrium distribution function,  $f_1 \propto |\mathbf{E}|$ , and  $f_2 \propto |\mathbf{E}|^2$ . The directed electric current along the structure edge is then given by

$$J_y = 4e \int_0^\infty dx \sum_{\mathbf{k}} f_2(\mathbf{k}, x) v_y. \quad (37)$$

Here, the factor 4 accounts for the spin and valley degeneracy.

As a model, we consider the simplest form of collision integral,

$$Q\{f(\mathbf{k}, x, t)\} = -\frac{f(\mathbf{k}, x, t) - f_0(\varepsilon_{\mathbf{k}})}{\tau}, \quad (38)$$

and assume the diffusive elastic scattering of carriers at the edge, which implies that  $f(\mathbf{k}, 0, t)$  is independent of the direction of  $\mathbf{k}$  for  $v_x > 0$  and  $\int f(\mathbf{k}, 0, t) v_x d\varphi_{\mathbf{k}} = 0$ .

To first order in the electric field, solution of Eq. (35) with the above boundary conditions has the form

$$f_1(\mathbf{k}, x) = -\frac{e\tau f'_0}{1 - i\omega\tau} [\mathbf{E}_0 \cdot \mathbf{v} - (\mathbf{E}_0 \cdot \mathbf{v} + \frac{\pi}{4} E_{0,x} v) \exp\left(-\frac{1 - i\omega\tau}{v_x \tau} x\right) \Theta(v_x)], \quad (39)$$

where  $f'_0 = df_0(\varepsilon)/d\varepsilon$  and  $\Theta(v_x)$  is the step function equal to 1 and 0 for  $v_x > 0$  and  $v_x < 0$ , respectively.

The equation for the second-order correction  $f_2(\mathbf{k}, x)$  to the distribution function, which gives rise to  $dc$  electric current, assumes the form

$$v_x \frac{\partial f_2(\mathbf{k}, x)}{\partial x} + \frac{2e}{\hbar} \text{Re} \left[ \mathbf{E}_0^* \frac{\partial f_1(\mathbf{k}, x)}{\partial \mathbf{k}} \right] = -\frac{f_2(\mathbf{k}, x)}{\tau}, \quad (40)$$

which yields

$$\int_0^\infty f_2(\mathbf{k}, x) dx = v_x \tau [f_2(\mathbf{k}, 0) - f_2(\mathbf{k}, \infty)] - \frac{2e\tau}{\hbar} \int_0^\infty \text{Re} \left[ \mathbf{E}_0^* \frac{f_1(\mathbf{k}, x)}{d\mathbf{k}} \right] dx. \quad (41)$$

By using Eqs. (37) and (41) we derive for the edge electric current

$$J_y = -8 \frac{e^3 \tau^3}{\hbar} \sum_{\mathbf{k}} \text{Re} \left\{ \frac{v_x v_y \mathbf{E}_0^* d[(\mathbf{E}_0 \cdot \mathbf{v}) f'_0]}{1 - i\omega\tau d\mathbf{k}} \right\} \quad (42)$$

$$+ \frac{v_y \mathbf{E}_0^*}{(1 - i\omega\tau)^2} \frac{d}{d\mathbf{k}} \left[ (\mathbf{E}_0 \cdot \mathbf{v} + \frac{\pi}{4} E_{0,x} v) f_0' v_x \right] \Theta(v_x),$$

where the above two contributions to the current stem from the first and second terms on the right-hand side of Eq. (41), respectively.

In graphene, the electron kinetic energy and velocity are given by  $\varepsilon_{\mathbf{k}} = \hbar v |\mathbf{k}|$  and  $\mathbf{v} = v \mathbf{k}/k$ , respectively. Therefore, we obtain for the edge photocurrent contribution from the electrons

$$J_y = - \frac{e^3 \tau^3 v^2 f_0(0)}{2\pi \hbar^2 [1 + (\omega\tau)^2]} \left[ \left( 1 + \frac{7}{6} \frac{1 - (\omega\tau)^2}{1 + (\omega\tau)^2} \right) \times (E_{0,x} E_{0,y}^* + E_{0,y} E_{0,x}^*) + \frac{10}{3} \frac{\omega\tau}{1 + (\omega\tau)^2} i [\mathbf{E}_0 \times \mathbf{E}_0^*]_z \right]. \quad (43)$$

Similarly to the case of the photon drag effect the valence band holes contribution to the photocurrent can be obtained from Eq. (43) by the replacement  $e \rightarrow -e$  and  $f_0(0) \rightarrow f_0^{(\text{hole})}(0) = [1 - f_0(0)]$ . Taking into account both electron and hole currents we obtain that the total electric current emerging at the sample edge is given by Eq. (43), where  $f_0(0)$  should be replaced by  $[2f_0(0) - 1]$ .

The dependences of the edge photocurrent (43) on the angles  $\varphi$  and  $\alpha$  are given by

$$J_y(\varphi) \propto \frac{C_l}{2} \sin 4\varphi + C_c \sin 2\varphi, \quad (44)$$

$$J_y(\alpha) \propto C_l \sin 2\alpha. \quad (45)$$

The microscopic theory for the edge photocurrents is in a good agreement with experimental results. At normal incidence the observed photoresponse is, according to Eq. (44), a sum of the contributions proportional to function  $\sin 2\varphi$  and  $B \sin(4\varphi) + C \cos(4\varphi) \propto \sin(4\varphi + \xi)$ , see Fig. 2(a). The additional phase  $\xi$  in experimental dependences results from the arbitrary orientation of the sample edges. Moreover, the dependence of the experimental data of the azimuthal angle  $\alpha$ , Fig. 2(b), demonstrates  $\sin 2\alpha$  and  $\cos 2\alpha$  behavior in agreement with Eq. (45). Hence, helicity driven and linear polarization dependent photocurrents in graphene are well described at the normal incidence by our model of edge effects.

## VI. SUMMARY

To summarize, our observations clearly demonstrate that the irradiation of monolayer graphene flakes results in directed electric currents of different origins. In all our measurements a substantial contribution to the photocurrent is driven by the photon helicity. It can be separated into the contribution resulting from normal incidence and the one from oblique incidence. While the contribution from oblique incidence is related to the bulk material and results from the transfer of the photon angular and linear momentum to free carriers, the effect at normal incidence is caused by the sample edges and vanishes in the bulk material. Our theory describes the helicity driven as well as the linear-polarization driven photocurrents in the classical limit where the radiation frequency is smaller compared to the characteristic energy of the carriers. The treatment of the general case, where interband transitions should be taken into account, is a future task.

*Note added.* At the day of the submission of this manuscript, Entin et al. have published a pre-print<sup>49</sup> devoted to the theory of the linear photon drag effect in graphene. Unlike in Ref. 49, where the direct interband absorption of linearly polarized light is considered, here we present results of mutual experimental and theoretical studies of the photon drag effect in graphene under indirect intrasubband optical transitions for both linear and circular polarizations, with emphasis on helicity-dependent photocurrents.

## Acknowledgments

We thank J. Fabian, V.V. Bel'kov, J. Kamann, and V. Lechner for fruitful discussions. The support from the DFG, the Linkage Grant of IB of BMBF at DLR, RFBR, President grant for young scientists and the "Dynasty" Foundation – ICFPM is gratefully acknowledged.

<sup>1</sup> K.S. Novoselov, A.K. Geim, S.V. Morozov, D. Jiang, Y. Zhang, S.V. Dubonos, I.V. Grigorieva, and A.A. Firsov, *Science* **306**, 666 (2004).

<sup>2</sup> K.S. Novoselov, A.K. Geim, S.V. Morozov, D. Jiang, M.I. Katsnelson, I.V. Grigorieva, S.V. Dubonos, and A.A. Firsov, *Nature* **438**, 197 (2005).

<sup>3</sup> Y. Zhang, Y.-W. Tan, H.L. Stormer, and P. Kim, *Nature* **438**, 201 (2005).

<sup>4</sup> E. McCann, K. Kechedzhi, V.I. Fal'ko, H. Suzuura, T. Ando, and B.L. Altshuler, *Phys. Rev. Lett.* **97**, 146805

(2006).

<sup>5</sup> F.V. Tikhonenko, D.W. Horsell, R.V. Gorbachev, and A.K. Savchenko, *Phys. Rev. Lett.* **100**, 056802 (2008).

<sup>6</sup> A.K. Geim and K.S. Novoselov, *Nature Mat.* **6**, 183 (2007).

<sup>7</sup> M.I. Katsnelson, K.S. Novoselov, and A.K. Geim, *Nature Phys.* **2**, 620 (2006).

<sup>8</sup> O. Klein, *Z. Phys.* **53**, 157 (1929).

<sup>9</sup> A.F. Young and P. Kim, *Nature Phys.* **5**, 222 (2009); N. Stander, B. Huard, and D. Goldhaber-Gordon, *Phys. Rev. Lett.* **102**, 026807 (2009).

- <sup>10</sup> A. Rycerz, J. Tworzydło, and C.W.J. Beenakker, *Nature Phys.* **3**, 172 (2007).
- <sup>11</sup> T. Oka and H. Aoki, *Phys. Rev. B* **79**, 081406(R) (2009).
- <sup>12</sup> W. Yao, D. Xiao and Q. Niu, *Phys. Rev. B* **77**, 235406 (2008).
- <sup>13</sup> D.S.L. Abergel, T. Chakraborty, *Appl. Phys. Lett.* **95**, 062107 (2009).
- <sup>14</sup> S.D. Ganichev and W. Prettl, *J. Phys.: Condens. Matter* **15**, R935 (2003).
- <sup>15</sup> E.L. Ivchenko, *Optical Spectroscopy of Semiconductor Nanostructures* (Alpha Science Int., Harrow, UK, 2005).
- <sup>16</sup> S.D. Ganichev and W. Prettl, *Intense Terahertz Excitation of Semiconductors* (Oxford Univ. Press, Oxford, 2006).
- <sup>17</sup> E.L. Ivchenko and S.D. Ganichev, *Spin Photogalvanics in Spin Physics in Semiconductors*, ed. M.I. Dyakonov, (Springer, Berlin, 2008).
- <sup>18</sup> S.D. Ganichev, S.N. Danilov, J. Eroms, W. Wegscheider, D. Weiss, W. Prettl, and E.L. Ivchenko, *Phys. Rev. Lett.* **86**, 4358 (2001).
- <sup>19</sup> S.D. Ganichev, E.L. Ivchenko, V.V. Bel'kov, S.A. Tarasenko, M. Sollinger, D. Weiss, W. Wegscheider, and W. Prettl, *Nature (London)* **417**, 153 (2002).
- <sup>20</sup> S.A. Tarasenko, *JETP Lett.* **85**, 182 (2007).
- <sup>21</sup> P. Olbrich, S.A. Tarasenko, C. Reitmaier, J. Karch, D. Plohmann, Z.D. Kvon, and S.D. Ganichev, *Phys. Rev. B* **79**, 121302(R) (2009).
- <sup>22</sup> P. Olbrich, E.L. Ivchenko, T. Feil, R. Ravash, S.D. Danilov, J. Allerdings, D. Weiss, and S.D. Ganichev, *Phys. Rev. Lett.* **103**, 090603 (2009).
- <sup>23</sup> E.L. Ivchenko and G.E. Pikus, in *Problems of Modern Physics* (in Russian), eds. V.M. Tuchkevich and V.Ya. Frenkel (Nauka, Leningrad, 1980), p. 275 [English translation: *Semiconductor Physics*, eds. V.M. Tuchkevich and V.Ya. Frenkel (Cons. Bureau, New York, 1986), p. 427].
- <sup>24</sup> V.I. Belinicher, *Fiz. Tverd. Tela* **23**, 3461 (1981) [*Sov. Phys. Solid State* **23**, 2012 (1981)].
- <sup>25</sup> V.A. Shalygin, H. Diehl, Ch. Hoffmann, S.N. Danilov, T. Herrle, S.A. Tarasenko, D. Schuh, Ch. Gerl, W. Wegscheider, W. Prettl, and S.D. Ganichev, *Pis'ma Zh. Exp. Teor. Fiz.* **84**, 666 (2006) [*JETP Lett.* **84**, 570 (2006)].
- <sup>26</sup> T. Hatano, T. Ishihara, S.G. Tikhodeev, and N.A. Gippius, *Phys. Rev. Lett.* **103**, 103906 (2009).
- <sup>27</sup> R. Hertel, *Journ. Magn. Magn. Mat.* **303**, L1 (2006).
- <sup>28</sup> J. Eroms and D. Weiss, *New J. Phys.* **11**, 095021 (2009).
- <sup>29</sup> U. Stöberl, U. Wurstbauer, W. Wegscheider, D. Weiss, and J. Eroms, *Appl. Phys. Lett.* **93**, 051906 (2008).
- <sup>30</sup> In spite of the fact that care was taken to align the radiation propagation direction most closely parallel to the line connecting the contacts the slight deviations are possible since the invisible radiation and the small sample size prevent a full control of the geometry.
- <sup>31</sup> B.I. Sturman and V.M. Fridkin, *The photovoltaic and photorefractive effects in non-centrosymmetric materials*, Gordon and Breach (1992).
- <sup>32</sup> F. Bassani and G. Pastori Parravicini, *Electronic states and optical transitions in solids*, Pergamon Press (1975).
- <sup>33</sup> H.E.M. Barlow, *Proc. IRE* **46**, 1411 (1958).
- <sup>34</sup> V.I. Perel' and Ya.M. Pinskii, *Fiz. Tverd. Tela* **15**, 996 (1973) [*Sov. Phys. Solid State* **15**, 688 (1973)].
- <sup>35</sup> N.A. Brynskikh, A.A. Grinberg, and E.Z. Imamov, *Fiz. Tekh. Poluprovodn.* **5**, 1735 (1971) [*Sov. Phys. Semicond.* **5**, 1516 (1972)].
- <sup>36</sup> I.D. Yaroshetskii and S.M. Ryvkin, *The Photon Drag of Electrons in Semiconductors* (in Russian), in *Problems of Modern Physics* ed. V.M. Tuchkevich and V.Ya. Frenkel (Nauka, Leningrad, 1980), pp. 173-185 [English translation: *Semiconductor Physics*, ed. V.M. Tuchkevich and V.Ya. Frenkel (Cons. Bureau, New York, 1986), pp. 249-263].
- <sup>37</sup> A.F. Gibson and M.F. Kimmitt, *Photon Drag Detection, in Infrared and Millimeter Waves, Vol. 3, Detection of Radiation*, ed. K.J. Button (Academic Press, New York, 1980), pp. 181-217.
- <sup>38</sup> S.D. Ganichev, E.L. Ivchenko, R.Ya. Rasulov, I.D. Yaroshetskii, and B.Ya. Averbukh, *Fiz. Tverd. Tela* **35**, 198 (1993) [*Phys. Solid State* **35**, 104 (1993)].
- <sup>39</sup> V.M. Shalaev, C. Douketis, J.T. Stuckless, and M. Moskovits, *Phys. Rev. B* **53**, 11388 (1996).
- <sup>40</sup> M.Ya. Amusia, A.S. Baltenkov, L.V. Chernysheva, Z. Felfi, A.Z. Msezane, and J. Nordgren, *Phys. Rev. A* **63**, 052512 (2001).
- <sup>41</sup> V.K. Dolmatov, D. Bailey, and S.T. Manson, *Phys. Rev. A* **72**, 022718 (2005).
- <sup>42</sup> J.E. Goff and W. L. Schaich, *Phys. Rev. B* **56**, 15421 (1997).
- <sup>43</sup> V.L. Gurevich and R. Laiho, *Phys. Rev. B* **48**, 8307 (1993); V.L. Gurevich and R. Laiho, *Phys. Solid State* **42**, 1807 (2000).
- <sup>44</sup> M.M. Glazov, E.L. Ivchenko, and S.A. Tarasenko, to be published.
- <sup>45</sup> We note that ripples and other imperfections generally can also reduce the symmetry and yield a photocurrent. In our samples, however, AFM images do not demonstrate the presence of ripples, and, to our opinion, it is likely that the effect comes from edges.
- <sup>46</sup> We note that the microscopic mechanism of the edge current is similar to the surface photogalvanic effect observed in bulk materials<sup>43,47,48</sup>.
- <sup>47</sup> L.I. Magarill and M.V. Entin, *Fiz. Tverd. Tela* **21**, 1280 (1979) [*Sov. Phys. Solid State* **21**, 743 (1979)].
- <sup>48</sup> V.L. Alperovich, V.I. Belinicher, V.N. Novikov, and A.S. Terekhov, *Pis'ma v Zh. Eksp. Teor. Fiz.* **31**, 581 (1980) [*JETP Lett.* **31**, 547 (1980)].
- <sup>49</sup> M.V. Entin, L.I. Magarill, and D.L. Shepelyansky, preprint arXiv:1002.0679v1 (2010).